Earth and Planetary Science Letters 609 (2023) 118088

Contents lists available at ScienceDirect

Earth and Planetary Science Letters

journal homepage: www.elsevier.com/locate/epsl

The development of multiple phases of superposed rifting in the Turkana Depression, East Africa: Evidence from receiver functions

C.S. Ogden [a,b,*], I.D. Bastow [a], C. Ebinger [c], A. Ayele [d], R. Kounoudis [a], M. Musila [c], R. Bendick [e], N. Mariita [f], G. Kianji [g], T.O. Rooney [h], G. Sullivan [c], B. Kibret [d]

[a] Department of Earth Science and Engineering, Imperial College, London, UK
[b] School of Geography, Geology and the Environment, University of Leicester, Leicester, UK
[c] Department of Earth and Environmental Sciences, Tulane University, New Orleans, USA
[d] Institute of Geophysics, Space Science and Astronomy, Addis Ababa University, Ethiopia
[e] Department of Geosciences, University of Montana, Missoula, MT, USA
[f] Geothermal Energy Training and Research Institute, Dedan Kimathi University of Technology, Nyeri, Kenya
[g] Department of Earth and Climate Sciences, University of Nairobi, Kenya
[h] Department of Earth and Environmental Science, Michigan State University, USA

ARTICLE INFO

Article history:
Received 26 September 2022
Received in revised form 24 February 2023
Accepted 26 February 2023
Available online 14 March 2023
Editor: J.P. Avouac

Keywords:
crustal thickness
bulk crustal composition
East African Rift
Turkana Depression
H-κ stacking
receiver functions

ABSTRACT

The Turkana Depression in Eastern Africa separates the elevated plateaus of East Africa to the south and Ethiopia-Yemen to the north. It remains unclear whether the Depression lacks dynamic mantle support, or if the entire East Africa region is dynamically supported and the Depression compensated isostatically by thinned crust. Also poorly understood is how Miocene-Recent extension has developed across the Depression, connecting spatially separated magmatic rift zones in Ethiopia and Kenya. Receiver function analysis is used to constrain Moho depth and bulk-crustal V_P/V_S ratio below new seismograph networks in the Depression, and on the northern Tanzania craton. Crustal thickness is ~40 km below northern Uganda and 30–35 km below southern Ethiopia, but 20–30 km below most of the Depression, where mass-balance calculations reveal low elevations can be explained adequately by crustal thinning alone. Despite the fact that magmatism has occurred for 45 Ma across the Depression, more than 15 Ma before East African Rift (EAR) extension initiated, bulk crustal V_P/V_S across southern Ethiopia and the Turkana Depression (~1.74) is similar to that observed in areas unaffected by Cenozoic rifting and magmatism. Evidence for voluminous lower crustal intrusions and/or melt, widespread below the Ethiopian rift and Ethiopian plateau to the north, is therefore lacking. These observations, when reviewed in light of high stretching factors ($\beta \leq 2.11$), suggest Cenozoic extension has been dominated until recently by faulting and plate stretching, rather than magma intrusion, which is likely an incipient process, operating directly below seismically-active Lake Turkana. Early-stage EAR basins to the west of Lake Turkana, with associated stretching factors of $\beta \approx 2$, formed in crust only moderately thinned during earlier rifting episodes. Conversely, ~23 km-thick crust beneath the Kino Sogo Fault Belt (KSFB) has small offset faults and thin sedimentary strata, suggesting almost all of the observed stretching occurred in Mesozoic times. Despite the KSFB marking the shortest path between focused extensional zones to the north and south, seismicity and GPS data show that modern extension is localized below Lake Turkana to the west. Failed Mesozoic rift zones, now characterized by thinned crust and relatively refractory mantle lithosphere, are being circumnavigated, not exploited by EAR rifting.

1. Overview

The low-lying Turkana Depression marks a ~500 km section of the East Africa Rift (EAR) separating the uplifted Ethiopian (~2.5 km) and East African (~1.5 km) plateaus (Fig. 1). The reasons for the Depression's low elevation are debated—specifically whether it is due to a break in mantle dynamic support between the two uplifted plateaus (e.g., Rogers et al., 2000), or crustal thinning above a broadly dynamically-uplifted region (e.g., Ebinger and Sleep, 1998). Since 1 Ma, magmatic extension has reached crustal depths along the axis of the Lake Turkana basin (Muirhead et al., 2022; Rooney et al., 2022), but the extent to which this process has

* Corresponding author.
E-mail address: chris.ogden@leicester.ac.uk (C.S. Ogden).

https://doi.org/10.1016/j.epsl.2023.118088

operated during earlier stages of EAR development is unknown. Similarly, the extent to which episodes of Eocene-to-Miocene flood basaltic volcanism, and later smaller volume magmatic episodes (e.g., Rooney, 2020a; Steiner et al., 2021), have affected bulk crustal composition in the Turkana Depression is also unconstrained.

Another fundamental question posed by the Turkana region concerns how focused rifting in northern Kenya and southern Ethiopia have linked across the Depression. Geodetic data indicate 40–100% of present-day strain is localized across faults and eruptive volcanic centers in and around Lake Turkana (Knappe et al., 2020). Yet Lake Turkana does not chart the shortest path between present day active extension in the Suguta Valley in the northern Eastern Rift and the Chew Bahir rift of southernmost Ethiopia (Fig. 1b). Recent attempts to study the development of EAR extension across the Depression have adopted numerical and analog modelling approaches (Brune et al., 2017; Corti et al., 2019) that proceed on the assumption that the Depression was initially a homogeneous block of previously-thinned crust, with synchronous development of extensional zones across the entire Depression. Yet, strain has migrated eastward over the past 25 My, and gravity (e.g., Sippel et al., 2017), structural and stratigraphic data (e.g., Schofield et al., 2021) demonstrate that the Depression was likely a zone of high material heterogeneity following the complex but failed development of east-west-trending rifting during Cretaceous (130–80 Ma) and Paleogene (66–50 Ma) times. Crustal thinning and magmatic modification imparted during these extensional episodes would have been permanent, with potentially important implications for strain localization during subsequent Cenozoic EAR development.

Seismic constraints on crustal structure outside of the Lake Turkana Basin, where wide-angle seismic data confirm the crust is markedly thinned (~20 km: Mechie et al., 1997), are confined to low-resolution surface wave models that lack seismograph station coverage within the Depression (Benoit et al., 2006). To address these issues, we present a study of bulk crustal structure across the Turkana Depression and neighboring Tanzania craton. Within the Depression, broadband seismic data come from 32 broadband seismograph stations deployed during the US-UK-Ethiopian-Kenyan TRAILS (Turkana Rift Arrays Investigating Lithospheric Structure) project (e.g., Kounoudis et al., 2021). Data from an additional 20 seismic stations in northern Uganda sample the northern Tanzania craton, including the Proterozoic-age, intra-cratonic Aswa shear zone (Fig. 1b). We follow the modified H-κ stacking method of Ogden et al. (2019) to constrain Moho depth (H) and bulk crustal V_P/V_S ratio (κ) across the region (Fig. 1). In doing so, we place fundamental new constraints on crustal structure in a region of multiple superposed episodes of rifting.

2. Tectonic setting

The Archean Tanzania craton (Fig. 1) forms the nucleus of the uplifted East African plateau and is surrounded by several Proterozoic mobile belts. The main collisional phase, the East African Orogeny (700–550 Ma), comprized protracted island-arc and microcontinent accretion, including the suturing of the Saharan metacontinent with the northern Tanzania craton along the Aswa shear zone (e.g., Fritz et al., 2013). Proterozoic ophiolites and sutures in southern Ethiopia mark locations of past subduction (e.g., Emishaw and Abdelsalam, 2019; Rooney, 2020a). Since the East African Orogeny, the Turkana Depression has experienced three distinct rifting phases: during the Cretaceous (130–80 Ma), Paleogene (66–50 Ma), and Miocene–Recent (25–0 Ma; e.g., Morley et al., 1992; Ebinger et al., 2000). The Mesozoic, mostly amagmatic, WNW-ESE-trending Anza and South Sudan rifts (Fig. 1a), constitute failed rifting associated with the Central African Rift System and opening of the Indian Ocean (e.g., Wilson and Guiraud, 1992).

Episodes of magmatism of varying volume, spatial and temporal extent have affected southern Ethiopia and the Turkana Depression throughout Cenozoic times. Pre-rift Eocene flood basalt magmatism occurred in southern Ethiopia at ~35–45 Ma but reached only as far south as ~5.5°N to the east of Lake Turkana; west of the lake, it is evidenced further south, near seismograph station KAEK (Fig. 1b; e.g., Steiner et al., 2021). Along the eastern flank of the Tanzania craton, 32 Ma carbonatites are associated with initial heating and metasomatism at the steep craton edge, localising magmatism and strain during Cenozoic rifting (Muirhead et al., 2020). Subsequently, magmatism migrated eastward during the Miocene, concomitant with the development of 3–4 sub-parallel NNE-striking half graben basins (Fig. 1b), including the Lake Turkana rift basin (e.g., Morley et al., 1992; Ebinger et al., 2000). Turkana records three periods of magmatism and related extension at ca. 20 Ma, 12 Ma, and 4 Ma and similar activity migrated outward from Turkana to other parts of the East Africa Rift System (EARS) (e.g., Rooney, 2020a). The Pliocene-age, Stratoid phase, Gombe group lavas erupted during the last of these three phases and span a broad region to the east of Lake Turkana (Fig. 1b), but are volumetrically less-significant (e.g., Haileab et al., 2004) than the earlier flood basalt episodes. The dominant topographic features of the eastern Turkana Depression are the large, Plio-Pleistocene age, mostly un-faulted, shield volcanoes of Huri Hills, Marsabit and Kulal which erupted spatially extensive basalt flows (e.g., Key et al., 1987). Analysis of the very youngest erupted products along the axis of Lake Turkana suggests that similar magmatic extension to that observed below the magmatically-mature sectors of the Main Ethiopian Rift (MER) to the north may have initiated below the lake since ~1 Ma (e.g., Rooney et al., 2022).

Within the uplifted Ethiopian and East African plateaus, faulting and magmatism have localized since ~5 Ma to 80–100 km-wide rift basins in the MER to the north of the Turkana Depression, and 60–80 km-wide zones in the Eastern and Western rifts to the south (Fig. 1). In the central and northern MER, within the basin bounded by Miocene border faults, the rift floor comprises a series of Quaternary-to-Recent aligned volcanic centers cut by small offset normal fault systems, referred to as magmatic segments, where ~80% of present-day strain is believed to be accommodated (Ebinger and Casey, 2001). Precisely how Cenozoic strain has developed in southernmost Ethiopia immediately to the north of the failed Cretaceous and Paleogene rift zones is poorly understood, however. Extension is thought to have started in early Miocene times in the Chew Bahir Rift (e.g., Ebinger et al., 2000). Fault development since ~3 Ma in the Ririba Rift to the east is associated with a maximum cumulative displacement of ~160 m (Corti et al., 2019), but its relationship with extensional zones to the north and south is unconstrained by geological data. Similarly, the Kino Sogo Fault Belt (KSFB), which lies between the deep basins beneath Lake Turkana in the west and the low-relief Ririba Rift to the north east, is associated with minor offset (<100 m), 3 Ma–Recent faults with associated extension rates of ~1 mm/yr and $\beta \approx 1.01$ (Vétel et al., 2005), but its relationship to extensional zones to the north and south remains unclear.

3. Previous geophysical work

A consensus has emerged among the mantle tomographic imaging community that East Africa is underlain by a broad (500 km-wide) slow wavespeed structure originating at the core-mantle boundary beneath southern Africa, impinging on the base of the lithosphere somewhere in the vicinity of Kenya/Ethiopia and the Red Sea/Gulf of Aden (e.g., Ritsema et al., 2011). Most recently, Kounoudis et al. (2021) used regional body-wave tomographic imaging using project TRAILS data to assert that there is no evidence for a break in buoyant dynamic support in the upper mantle

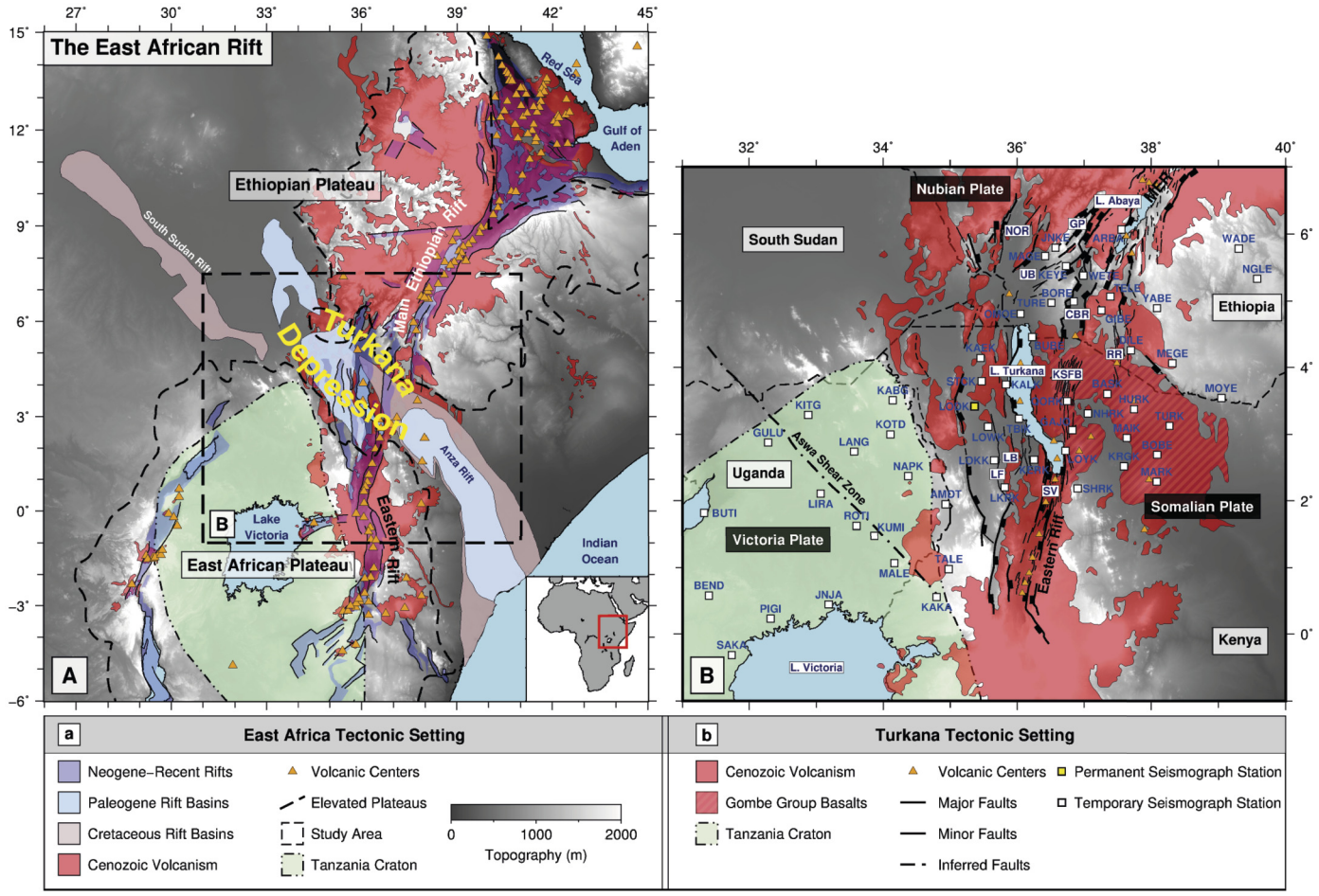

Fig. 1. (a) Tectonics of the Cenozoic East African Rift System. The Turkana Depression is the low-lying region between the elevated Ethiopian and East African Plateaus to the north and south, respectively. Paleogene and Cretaceous rift basins that developed during Mesozoic rifting are also shown (Hendrie et al., 1994). Orange triangles are Holocene and Pleistocene volcanic centers. **(b)** Our study area, including the location of major (thick solid lines), minor (thin solid lines), and inferred (dashed lines) Cenozoic faults after Brune et al. (2017) and Moore and Davidson (1978); volcanic regions are after Rooney et al. (2017) and Rooney (2020a). Outline of Tanzania Craton from Rooney (2020b). CBR: Chew Bahir Rift. GP: Gofa Province. KSFB: Kino Sogo Fault Belt. LB: Lokichar Basin. LF: Lokichar Fault. NOR: North Omo Rift. RR: Ririba Rift. SV: Suguta Valley. UB: Usno Basin.

below the Turkana Depression. However, they noted that low velocity zones at mantle lithospheric depths are not localized to one or more narrow rift valleys, as in the MER to the north (e.g., Bastow et al., 2005) and Eastern Rift to the south (Park and Nyblade, 2006), with the implication that currently-active magma-assisted rifting may not yet be underway below the Turkana Depression. A surprising observation in the Kounoudis et al. (2021) P-wave model was a relatively narrow (~50 km-wide) high wavespeed band in southern Ethiopia, interpreted as refractory Proterozoic lithospheric mantle that likely influenced Mesozoic (Anza) and Cenozoic (EAR) strain localization. Until the deployment of the XW seismograph network in northern Uganda, the only bulk-crustal constraints available in the region came from the joint receiver function and surface-wave study of Tugume et al. (2013) who found, to the south of the Aswa shear zone, a crustal thickness of 36–45 km for northern Uganda with a ~3 km thick, high-shear-wave-velocity lower crustal layer. Subsequently, Wang et al. (2022) presented joint inversion results to the north of the Aswa shear zone, across which they found no notable changes in crustal properties. They found V_P/V_S ratios of 1.76–1.82 with Moho depths in the range 34–38 km.

Wide-angle seismic constraints from the Kenya Rift International Seismic Project (KRISP; e.g., Mechie et al., 1997) revealed variations in crustal thickness and uppermost-mantle structure along the axis of the Eastern Rift, reaching northern Lake Turkana (e.g., Mechie et al., 1997). Moho depths of ~35 km and ~20 km are revealed beneath the East African Plateau and Lake Turkana respectively, with the latter attributed to widespread Cenozoic rifting (Mechie et al., 1997). The Rayleigh wave dispersion model of Benoit et al. (2006), calculated with no seismograph stations within the Depression, generally corroborated the KRISP constraints: shallow slow wavespeeds spanning the whole Depression suggest crustal thinning, with an average Moho depth of 25 ± 5 km.

To the north of the Turkana Depression in the central and northern MER sectors, wide-angle seismic profiles (Maguire et al., 2006), magnetotelluric studies (Whaler and Hautot, 2006), crustal tomography (e.g., Keranen et al., 2004) and gravity models (e.g., Cornwell et al., 2006) reveal that dense, fast wavespeed lower to mid-crustal material, interpreted as gabbroic intrusions, have accommodated significant extension without marked crustal thinning below a relatively narrow (~20 km-wide) in-rift zone of faulting and Quaternary magmatism that now accommodates ~80% of Nubia-Somalia plate separation. Corroborating this magma assisted rifting hypothesis, receiver function constraints on bulk crustal structure in the central and northern MER reveal elevated V_P/V_S ratios, in some cases >2, which strongly imply the presence of melt and new mafic material (Stuart et al., 2006). Receiver function constraints on crustal structure in the southern MER are limited, but Ogden et al. (2021) found $V_P/V_S \approx 1.7$ at station ARBA (Fig. 1), and suggested melt volumes are lower in this less magmatically-

evolved rift sector, away from major volcanic centers. This finding was consistent with the observation that strain in the southern MER is accommodated primarily along the western rift border fault (Kogan et al., 2012), not along shorter length-scale, in-rift faults associated with magmatic extension, as is the case in the central and northern MER sectors.

Analyzing receiver function data from seismograph stations immediately to the north, west, and east of the Ethiopian flood basalt province including near the Sudan border, Ogden et al. (2019) found bulk crustal V_P/V_S ratios of the order ~1.74, consistent with a paucity of melt and mafic material in the crust below these stations. Further, evidence for a sharp crust-mantle transition at all of these stations was cited as evidence that the 8–12 km-thick lower crustal intrusion layer observed below the flood-basalt-affected part of the Ethiopian plateau (Mackenzie et al., 2005) was lacking below these stations.

New and ongoing GNSS data show comparable plate opening velocities across the southern Turkana Depression as in the northern MER, with strain localized to <150 km wide basins and uplifted flanks (Knappe et al., 2020). However, geodetic data are too sparse to evaluate the current localization of strain across the 300 km-wide broadly-rifted zone in southern Ethiopia.

4. Data and methods

4.1. The TRAILS seismograph network

Seismograph deployments in the Turkana Depression and adjoining areas on the MER and Eastern Rift were lacking compared to the rest of the EAR until the TRAILS broadband seismograph network (Fig. 1) was deployed in 2019 (e.g., Kounoudis et al., 2021) comprising 34 Güralp CMG-ESP and CMG-3T instruments, with flat responses to periods of 60 s and 120 s, respectively (see Table S1 for station details). Additional data were sourced from permanent GEOFON station LODK (Fig. 1), and from seismic stations of the ZP, XW and XI networks in northern Uganda (see supplementary information for further network details). The combined seismic network of 52 seismograph stations has an average station spacing of ~30–50 km.

4.2. Teleseismic dataset

Seismograms for all earthquakes of magnitude >4 in the epicentral distance range 30-90° were selected for P receiver function analysis. Additionally, seismograms for magnitude >5.5 earthquakes in the epicentral distance range 60° + were selected for PP receiver functions. Seismograms were filtered using a Butterworth bandpass filter with corner frequencies 0.04 Hz and 3 Hz. Earthquake-station pairs were accepted for further analysis if the P-wave signal-to-noise ratio was >2, allowing 1729 acceptable-quality three component seismograms. For each earthquake-station pair, receiver functions were calculated using the time-domain iterative deconvolution method of Ligorrìa and Ammon (1999). This deconvolution method produces receiver functions in which the dominant frequency of the resulting receiver function is that of the Gaussian width. For example, a Gaussian of 0.8 corresponds to a low-pass filter of ~0.4 Hz; a Gaussian of 4.0 corresponds to a low-pass filter of ~2 Hz. For each earthquake-station pair we generate a suite of 17 receiver functions with Gaussian width factors of 0.8 to 4.0 with intervals of 0.2. Receiver functions with an iterative deconvolution variance (a cross-correlation of the original radial component with a radial component recalculated from the receiver function) of ≤80% were rejected automatically along with all other frequencies for that earthquake-station pair; receiver functions were then inspected manually to remove remaining poor quality traces. Stations with <6 remaining earthquake-station pairs were not analyzed, leaving 955 earthquake-station pairs (16,235 individual receiver functions) from 34 individual stations for subsequent H-κ stacking analysis.

4.3. Receiver functions and H-κ stacking

Teleseismic receiver functions capture P-to-S wave conversions produced at velocity contrasts such as the Moho, beneath seismograph stations (e.g., Ligorrìa and Ammon, 1999). The travel times of the Moho P-to-S conversion (Ps) and subsequent crustal reverberations ($PpPs$, $PpSs + PsPs$), are exploited routinely to glean information on the crustal thickness (H) and bulk crustal V_P/V_S (κ) via the H-κ stacking procedure of Zhu and Kanamori (2000). The method involves stacking amplitudes along predicted move-out curves for the Moho conversion and subsequent reverberations. The optimal H and V_P/V_S ratio is obtained by picking the parameters that maximise the stacking amplitude, $s(H,\kappa)$. In this linear stacking approach, s(H,κ) is defined as:

$$s(H,\kappa) = \sum_{j=1}^{N}\sum_{k=1}^{3} w_k r_j(t_k), \tag{1}$$

where r_j is the amplitude of the radial receiver function for the jth event sampled at times, t_k, for values of k between 1 and 3 corresponding to the predicted travel-times for $PpPs$ and $PsPs + PpSs$, respectively. N is the total number of receiver functions; w_k is the weighting factor for each of the phases. Alternatively, in a phase weighted stacking approach (Schimmel and Paulssen, 1997), designed to enhance coherent arrivals throughout the stack, the phase stack is defined first as:

$$c(H,\kappa) = \frac{1}{N}\sum_{j=1}^{N}\left|\sum_{k=1}^{3} exp[i\phi(t_k)]\right|/3, \tag{2}$$

where ϕ is the instantaneous phase at time t. The value of $c(H,\kappa)$ ranges from 0 for uncorrelated data and 1 for perfectly correlated data; it is then used to weight the H-κ stack:

$$s'(H,\kappa) = c^{v}\sum_{j=1}^{N}\sum_{k=1}^{3} w_k r_j(t_k). \tag{3}$$

The phase stack is essentially a filter between poorly-correlated and well-correlated data, with the sharpness controlled by the parameter v. Following Schimmel and Paulssen (1997), we assume $v = 2$.

The optimal combination of H and κ is taken to be where $s(H,\kappa)$ is a maximum; individual measurement errors in H and κ are calculated from the 95% contour of the $s(H,\kappa)$ surface. The choice of H-κ stacking input parameters including V_P, the values assigned to the phase weights, and the choice of stacking strategy: linear versus phase-weighted, can each exert strong control on the final result. So too can data parameters such as receiver function frequency content, and the subset of receiver functions to be stacked. To overcome this parameter sensitivity issue, we follow the adapted H-κ method of Ogden et al. (2019) that repeats the standard H-κ stacking method 1000 times, with H-κ input parameters and data parameters sampled randomly between geologically plausible limits, and using cluster analysis to select a final solution from the suite of individual H-κ estimates. In each repeat, one receiver function frequency is selected randomly, from the 0.4–2 Hz range, resulting in ~1/17th of the 1000 results corresponding to each individual frequency. If, after the 1000 repeats, a station does not have a stable result, we systematically remove the individual

Table 1
The ten criteria used for determining result quality following Ogden et al. (2019) and Ogden and Bastow (2022). F_{max} is the maximum frequency content in result calculation.

Number	Criterion
1	Cluster analysis selected H or κ lies within the boundaries of the H-κ grid space.
2	Errors for cluster analysis selected result are: <±2.5 km in H and <±0.05 in κ.
3	Standard deviation of H is <±2.5 km.
4	Standard deviation of κ is <±0.05.
5	Mean average ACE of the repeats with frequency less than F_{max} is >3.
6	Mode H and κ lie within the same cluster as the mean H and κ.
7	Summed amplitudes of Ps, $PpPs$ and $PsPs + PpSs$ are positive, positive, and negative, respectively.
8	Mean average cross-correlation of all receiver functions is >3.
9	Mean average IDVAR of the repeats with frequency less than F_{max} is >90%.
10	Mean H and κ for the linear stack lies within PWS's standard deviation and vica-versa.

results obtained using higher frequencies (starting from 2 Hz) until a stable result is achieved (e.g., Figs. S1 and S2). The maximum stable frequency is denoted F_{max}. If upper-crustal structure is relatively simple (i.e. no major intra-crustal velocity discontinuities are present), F_{max} can be an indicator of how sharp the Moho is (Ogden et al., 2019): a gradational Moho will only produce a stable H-κ result at lower frequencies. The standard deviation of H and κ from the $\leq$1000 H-κ measurements generallyrepresent larger, more realistic error estimates than individual H-κ results chosen via cluster analysis; they also incorporate uncertainties in V_P. We therefore refer to these mean values as the final result from hereon in. Ten quality control criteria (Table 1) are used to assess the reliability of H–κ stacking at a station. V_P ranges from 6.2–6.8 km/s for Tanzania craton stations, with a 5.9–6.5 km/s range used for Turkana Depression stations owing to slower P-wave velocities imaged by the KRISP project (e.g., Mechie et al., 1997).

Following Ogden and Bastow (2022), we pay particular attention to three receiver function quality indicators; amplitude comparison estimate (ACE), cross-correlation coefficient (CCC) and iterative deconvolution variance (IDVAR). Larger values of these analytics indicate a larger amplitude Ps conversion and/or receiver functions which are relatively simple with homogeneous crustal structure beneath a station. Conversely, decreased analytic values might indicate the presence of a more gradational Moho or back-azimuthally variable crustal structure beneath the station.

Stations for which H-κ stacking did not produce a reliable result, but which had receiver functions with sufficiently clear P_S conversions, were analyzed via simple P_S arrival time analysis: H was determined for each individual receiver function by manually picking t_1,

$$H = \left(t_1 \Big/ \left(\sqrt{\frac{1}{V_S^2} - p^2} - \sqrt{\frac{1}{V_P^2} - p^2} \right) \right), \tag{4}$$

with V_S calculated from a well-constrained V_P/V_S ratio from a nearby station and $V_P = 6.2$ km/s. Mean crustal thickness and an associated standard deviation were then calculated for the suite of receiver functions to determine an estimate of Moho depth at these stations. Cunningham and Lekic (2019) have demonstrated the success of a resonance removal filter in obtaining H-κ results at stations where oscillatory receiver functions result from <2.5 km-thick sedimentary layers. Adopting this strategy in our study yielded no additional H-κ results, perhaps owing to the deep ($\geq$3 km; e.g., Sippel et al., 2017) nature of the Cenozoic and Mesozoic age basins that exist across much of the Turkana Depression.

5. Results and comparison to previous studies

Of the 52 seismograph stations analyzed, 34 produce reliable H-κ stacking results (Fig. 3; Tables S1 and S2). Additionally, three stations were only reliable using the P_S picking method (Table S3). Stations located on the thickest sedimentary sequences (e.g. on the shores of Lake Turkana: BUBE, KALK, OMOE, TBIK; Chew Bahir: BORE) either do not have six acceptable receiver functions (Figs. S3 and S4) or consistently pass <5 criteria and yield fewer H-κ constraints than stations in southern Ethiopia and Uganda (Fig. 3). This scenario is exacerbated at stations situated directly on basalts which overlie 1–2 km-thick thick sedimentary sequences such as above large regions of the Anza Rift (e.g. BASK, BOBE, GAJO, KRGK, MAIK, NHRK; Figs. S3 and S4). Receiver function analytics are all high, implying high quality receiver functions (IDVAR), relatively high amplitude Ps conversions associated with a sharp Moho and relatively simple crustal structure (ACE), and high receiver function similarity (CCC) as a function of earthquake back-azimuth and epicentral distance (Fig. S5). Result plots for all reliable stations are found in Figs. S6–S38, stations with unreliable H-κ results are shown in Figs. S39–S41.

In Section 4.3, we detailed how a successful H-κ stacking result uses results obtained from receiver function frequencies $\leq F_{max}$. Thus, stable solutions (e.g., station DILE; Fig. 2) presented at 2 Hz are inherently also stable at 0.4 Hz. Fig. S1 illustrates how H-κ results stay consistent for each individual frequency for a station reliable at 2 Hz. Following Ogden et al. (2019), achieving a stable result at all frequencies up to and including 2 Hz suggests that the Moho discontinuity is likely sharp; stations that work at reduced frequencies either have a more gradational Moho discontinuity, or complex intra-crustal structure. Of the 34 reliable stations, only 15 have reliable H-κ solutions at reduced receiver function frequencies (e.g., station WETE; Figs. S2 and S37).

Moho depths are 35–40 km in central Uganda, with slightly thicker crust to the south of the Proterozoic (685–655 Ma) Precambrian Aswa shear zone (Saalmann et al., 2016) (e.g., H_{GULU} = 38.2 km) compared to the north of it (e.g., H_{KITG} = 35.1 km) on the Saharan metacraton. Performing joint inversion of surface waves and receiver functions using XW network data, Wang et al. (2022) found comparable crustal thicknesses of 34–38 km, but reported no discernible Moho step across the Aswa shear zone. The crust is ~40 km thick on the eastern Ethiopian plateau (e.g., H_{NGLE} = 38 km; Ogden et al., 2019), decreasing to 30-35 km in southern Ethiopia (e.g., H_{TELE} = 32.1 km), and 20-25 km near Lake Turkana (e.g., H_{LOYK} = 24.8 km), the Lokichar Basin (e.g., H_{LOKK} = 21.4 km), and the KSFB (e.g., H_{QORK} = 23.0 km) (Figs. 1, 3, and 4). The thicker crust of the elevated plateaus is consistent with the surface wave derived estimates of 38 km (Benoit et al., 2006) and the receiver function derived estimates of 38–41 km beneath the Rwenzori Belt of Uganda (Tugume et al., 2013).

Where coincident, our results corroborate the KRISP wide-angle seismic lines (e.g., Mechie et al., 1997), but we resolve more Moho topography than the surface wave study of Benoit et al. (2006), who found a ~25 km-thick crust across the Turkana Depression, thinning slightly to ~20 km beneath Lake Turkana. Our Moho depths in southern Ethiopia are shallower than those derived from recent gravity inversions (~43 km: Sippel et al., 2017).

Table 2
Stretching factors (β) for selected rifts and basins of East Africa and the Turkana Depression. MER rift crustal and sediment thickness from the EAGLE wide-angle seismic (Maguire et al., 2006) and gravity (Cornwell et al., 2006) profiles respectively. Kenya Rift crustal and sediment thickness from Braile et al. (1994). Reference station a: NGLE, b: TELE, c: AMDT. Sedimentary thicknesses; d: Cornwell et al. (2006), e: Doherty et al. (2013), f: Sippel et al. (2017), g: Vétel et al. (2005), h: Schofield et al. (2021), i: Morley et al. (1992), j: Braile et al. (1994).

Rift	β	Reference H (km)	Rift H (km)	Sed. Thick. (km)
MER	1.12	38[a]	35.8	2[d]
Chew Bahir Rift	1.35[b]–1.60[a]	32.1[b]–38.0[a]	25.4	1.6[e]
Ririba Rift	1.01	32.1[b]	31.7	0[f]
Anza Rift (N margin)	1.23–1.46	32.1[b]–38.0[a]	28.6	2.5[f]
Anza Rift	1.51–1.79	32.1[b]–38.0[a]	23	1.8[g]
Lake Turkana	2.07	34.2[c]	20	3.5[h]
Lokichar Basin	1.93	34.2[c]	21.2	3.5[h]
	2.11			5[i]
Kenya Rift	1.28	37	30.5	1.5[j]

Markedly thinned crust underlies Lake Turkana in northern Kenya, and the Chew Bahir Rift (CBR) in southern Ethiopia (e.g. WETE: 25.4 km; Fig. 4: B-B'). In contrast, the Ririba Rift and Usno Basin show no evidence for crustal thinning relative to other stations in southern Ethiopia. Moho depth in the Ririba Rift ($H_{DILE} = 31.7$ km) closely matches TELE (32.1 km), GIBE (32.1 km) and MEGE (34.1 km) which all lie outside of the Miocene-Recent rift zones. They all lie along the northern flank of the Mesozoic Anza Rift, and may have experienced uplift and flank-erosion prior to the East African rifting phase. Moho depth in the Usno Basin ($H_{MAGE} = 30.4$ km) is similar to that immediately outside it ($H_{KEYE} = 30.7$ km).

Moho depth at station TURK in the Anza Rift (31.3 km) is ~3–5 km shallower than the Ethiopian plateau (e.g. NGLE: 38 km) and some stations in southeastern Ethiopia (e.g. YABE: 34.4 km). To the west, crustal thickness decreases markedly across the Turkwell Escarpment from 34.2 km (station AMDT) to ~20 km in the Lokichar Basin (Fig. 4: D-D'). Moving northwards, the Lodwar region ($H_{LODK} = 25.4$ km) and the Lapurr Range ($H_{KAEK} = 31.1$ km) bounding the northwest shore of Lake Turkana have thicker crust than the Lokichar and Lake Turkana basins.

Several stations have bulk-crustal V_P/V_S <1.72 (Fig. 3); only one station (SHRK) has a significantly elevated V_P/V_S ratio of >1.9. This contrasts the surface wave study of Benoit et al. (2006), which found an average V_P/V_S ratio of ~1.81 for the Depression (Poisson's ratio of 0.28). Similarly-low V_P/V_S values (1.71–1.76) to those in Fig. 3c were found at stations off the eastern and western flanks of the Ethiopian flood basalt province by Ogden et al. (2019). Ogden et al. (2021) also found low a V_P/V_S ratio (1.70) at station ARBA in the southern MER.

Stretching factors (β) quantify the amount of plate stretching that has occurred in a phase of extension by calculating the ratio of crustal thickness of pre-deformed crust to that observed after extension, removing the thickness of basin infill. In each region of our study area we compare the observed crustal thickness to a reference station assumed to be unaffected by the extension phase of interest (Table 2).

For the MER and Eastern Rifts we interpret the seismic refraction profiles of Maguire et al. (2006) and Braile et al. (1994) to obtain β values of 1.12 and 1.28, respectively. In southern Ethiopia, we define β for the Chew Bahir Rift with a reference value of both station TELE and station NGLE depending on which station has crust representative of pre-extended crust in the region. This provides a β value of 1.35–1.60 for the Chew Bahir Rift. $\beta = 1.01$ for the Ririba Rift. The predominantly EAR affected extension zones of the Lokichar and Lake Turkana Basins are defined using the reference value of $H_{AMDT} = 34.2$ km for pre-Cenozoic crustal thickness at the edge of the Tanzania craton, resulting in $\beta = 1.93$ and $\beta = 2.07$, respectively. Additionally, Morley et al. (1992) determine 5 km of sediment in the Lokichar Basin, resulting in a slightly higher estimated stretching factor of 2.11. Finally we obtain two stretching factor estimates in the region predominantly affected by Anza Rifting, stations HURK (northern rift margin) and QORK (closer to the rift depocenter), assuming either Southern Ethiopia (TELE) or the Somalia Plate (NGLE; Ogden et al., 2019) as pre-extension crustal thickness references. Gravity models constrained by exploration well data show ~2.5 km of sediments below the these stations in the Anza basin (Sippel et al., 2017). Our 28.6 km crustal thickness estimate at HURK thus implies a lower bound estimate of $\beta = 1.23$–1.46 with a larger stretching factor of 1.51–1.79 calculated for QORK. These stretching estimates for the Anza Rift are minima because we lack crustal thickness estimates from stations corresponding to the centre of the basin inferred from gravity (Sippel et al., 2017).

6. Discussion

6.1. The low elevation of the Turkana Depression: crustal thinning or paucity of mantle dynamic support?

The number and location of mantle plumes below East Africa is debated. Initial geochemical insights showed that the radiogenic isotopic characteristics of basalts erupted in Afar exhibited differences to those found in the Kenya Rift — an observation attributed to the influence of two mantle plumes with distinct compositions (e.g., Rogers et al., 2000). This assertion was consistent with the existing helium isotopic data that showed contributions from a deep plume source only in the north of the EARS (e.g., Marty et al., 1996). In this geodynamic scenario, the low elevation of the Turkana Depression could be interpreted as evidence for a break in mantle dynamic support between the two plateaus. Subsequent isotopic observations from the Turkana Depression of a temporal transition between the two compositional plume types were used to argue for a heterogenous single plume (Furman et al., 2006). The subsequent discovery of a deeply-derived helium isotopic signature in southern portion of the EAR at Rungwe (e.g., Hilton et al., 2011; Halldórsson et al., 2014), the widespread occurrence of elevated mantle potential temperatures (Rooney et al., 2012), and the convergence of isotopic data in lavas from throughout the EARS on a single composition, support the notion that material rising from the African LLSVP contaminates the entire East African upper mantle (Rooney, 2020c). In Turkana, a plume-influenced upper mantle is currently supported by geochemical data from Quaternary basalts erupted in Lake Turkana. South Island lavas have trace element and isotopic values equivalent to plume-influenced lavas erupted further north in Ethiopia (Furman et al., 2006; Rooney

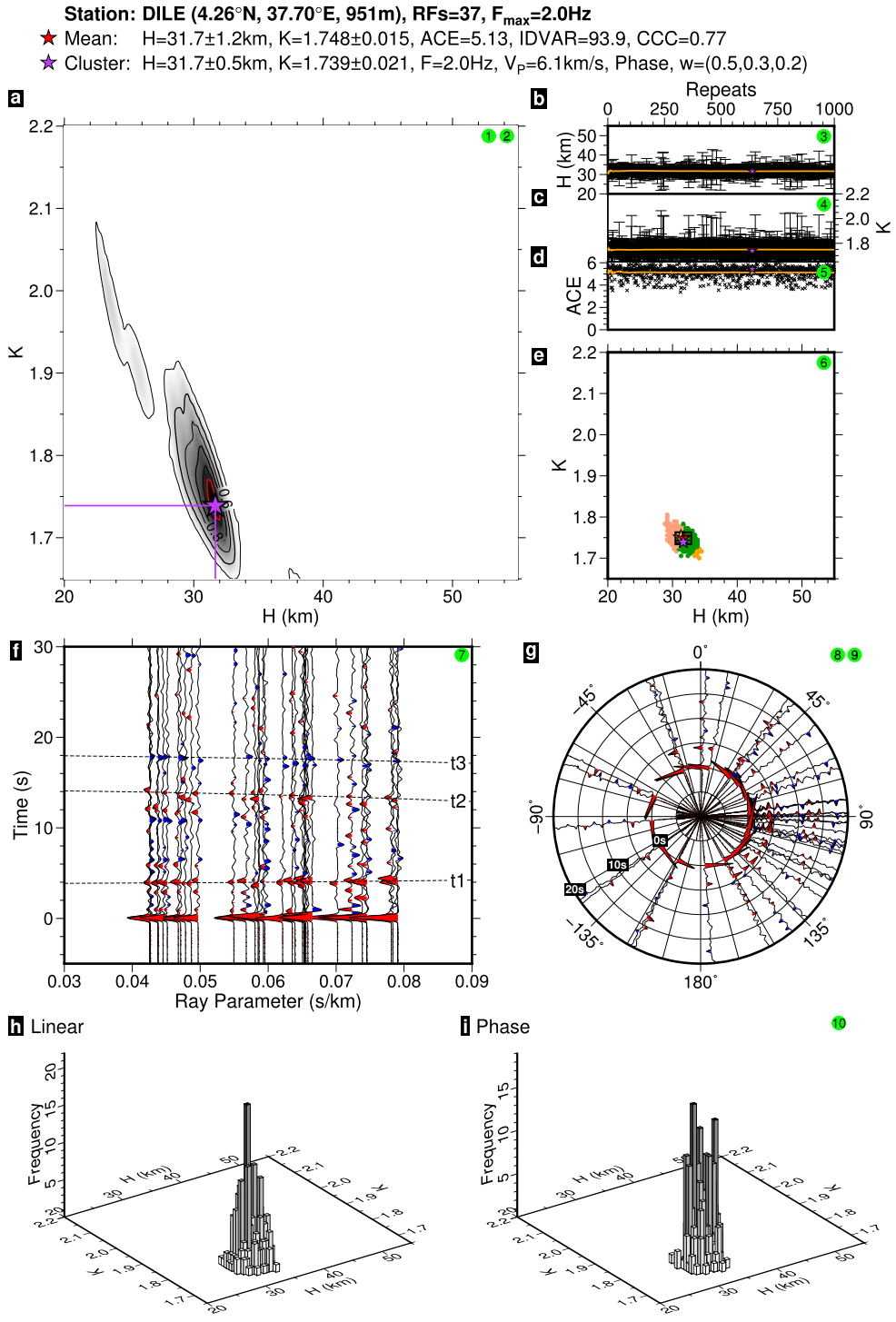

Fig. 2. Successful H-κ result for station DILE in southern Ethiopia (Fig. 1) for receiver function frequencies of $\leq$2 Hz. (a) The $s(H, \kappa)$ stacking surface associated with the result selected using hierarchical cluster analysis. Crustal thickness (b), V_P/V_S ratio (c), and ACE (d) for each of the 1000 H–κ solutions. (e) All 1000 H–κ solutions with color representing the cluster that a result is assigned to. The red star is the mean of H and κ from the 1000 repeats, the yellow star is the mode combination of H and κ, the purple star is the combination of H and κ selected by the cluster analysis and plotted in (a), the black box marks one standard deviation in H and κ. Accepted receiver functions plotted by horizontal slowness (f), and backazimuth (g), t_1, t_2 and t_3 denote the predicted arrival times from the selected H and κ solution in (a). The peaks/troughs are colored when their amplitude is >20% of the P arrival amplitude. (h and i) Distribution of linear and phase weighted stacking results.

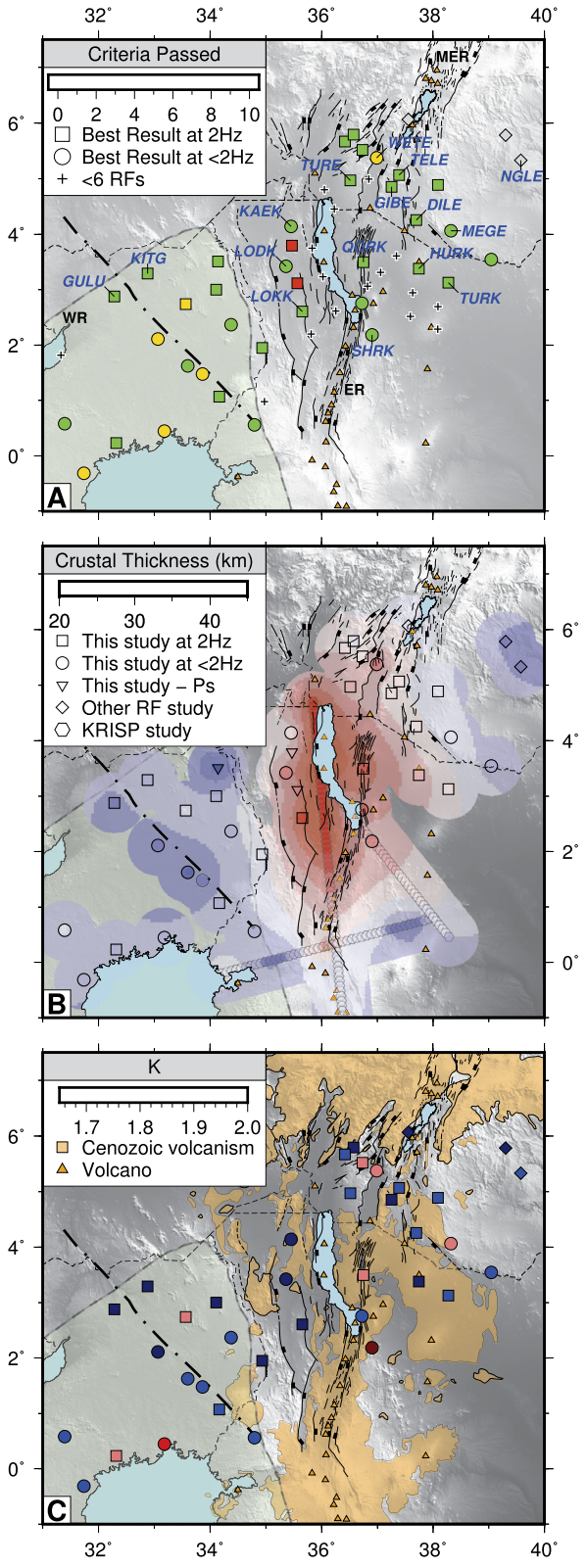

Fig. 3. a) Criteria passed for each station with six or more acceptable receiver functions. Dashed line is Aswa shear zone. MER: Main Ethiopian Rift. ER: Eastern Rift. WR: Western Rift. b) Crustal thickness below the study area. KRISP crustal thickness data are after (Mechie et al., 1997). c) V_P/V_S below each station where a result was reliable. Orange shading: volcanic regions after Rooney et al. (2017) and Rooney (2020a).

et al., 2022). These geochemical data thus support the presence of a plume-influenced upper mantle beneath the Turkana Depression, at least within the Turkana basin. Global (e.g., Ritsema et al., 2011; Boyce et al., 2021) and regional (Kounoudis et al., 2021) seismic tomographic imaging studies also support the view that mantle dynamic support is continuous below the region. Benoit et al. (2006) asserted that the region's low-lying nature is likely the result of crustal thinning, but drew their conclusions from surface wave analysis using data from seismograph stations exclusively outside of the Depression. Our station-by-station Moho depth constraints allow a more quantitative analysis of crustal thickness and elevation.

A striking observation in Fig. 3b is the widespread nature of thinned (<30 km) crust beyond the shores of Lake Turkana. Simple isostatic mass balance calculations (assuming Airy isostasy) can be used to quantify the support required beneath the Turkana Depression as compared to the neighboring eastern Ethiopian plateau (Fig. 5). Station NGLE is assumed representative of the un-rifted, dynamically-supported Ethiopian plateau (Fig. 3a, Table 3). Comparative mass balances use crustal thickness estimates and elevations for southern Ethiopia (station TELE), areas of the Anza Rift unaffected by Cenozoic rifting (station HURK) and Lake Turkana (Fig. 3b and Table 3).

Southern Ethiopia, the Anza Rift and Lake Turkana are, in fact, 635 m, 558 m and 554 m higher than expected, indicating that mantle dynamic support is abundant, not lacking below the Turkana Depression, as indicated in the recent mantle seismic tomographic study of Kounoudis et al. (2021). We therefore contend that the Turkana Depression's low lying nature is the result of crustal thinning, not a lack of dynamic support between two uplifted plateaus provided by distinct plumes.

6.2. Implications for magmatic crustal modification and magma-assisted rifting in the Turkana Depression

Assuming bulk crustal V_P/V_S ratios at stations in the southern MER (e.g., V_P/V_S = 1.70 at station ARBA; Ogden et al., 2021), and beyond the eastern and western flanks of the Ethiopian flood basalt province to the north (V_P/V_S ~ 1.74; Ogden et al., 2019) are representative of crust largely un-modified by Cenozoic magmatism, Fig. 3c reveals a striking lack of elevated bulk-crustal V_P/V_S ratios across the Turkana Depression, except below some isolated volcanic fields such as around station QORK (e.g., Vétel et al., 2005), where V_P/V_S = 1.8. This contrasts sharply much of Ethiopia to the north, where V_P/V_S ratios are often ≥1.8 (Stuart et al., 2006; Ogden et al., 2019) on account of both the voluminous flood basaltic magmatism there, and the well-established magma assisted rifting that is now ongoing in the central and northern sectors of the MER. Flood basaltic magmatism began in southern Ethiopia in Eocene times (~40 Ma; Davidson and Rex, 1980), but did not persist south of ~5.5°N to the east of Lake Turkana (Steiner et al., 2021). Younger episodes of magmatism to affect the Depression include the Pliocene-age Stratoid phase (e.g., Haileab et al., 2004). This was spatially widespread (500×100 km) east of Lake Turkana but small in volume, with thickness typically ≤100 m.

Of the stations situated directly on the large Pliocene-Pleistocene shield volcanoes in the Turkana Depression, only station HURK (Huri Hills) returns a reliable H-κ result: it displays a low V_P/V_S ratio ($\kappa = 1.692$), implying little present-day melt and mafic addition to the crust. On the other hand, where Pliocene-age volcanism around the Dilo volcanic field (Franceschini et al., 2020), and where young (~154 ka) volcanism has occurred around Mega, V_P/V_S is slightly above the regional background mean of ~1.74 at stations DILE (1.748) and MEGE (1.769), respectively. We cannot, of course, preclude the possibility that our receiver function data at stations

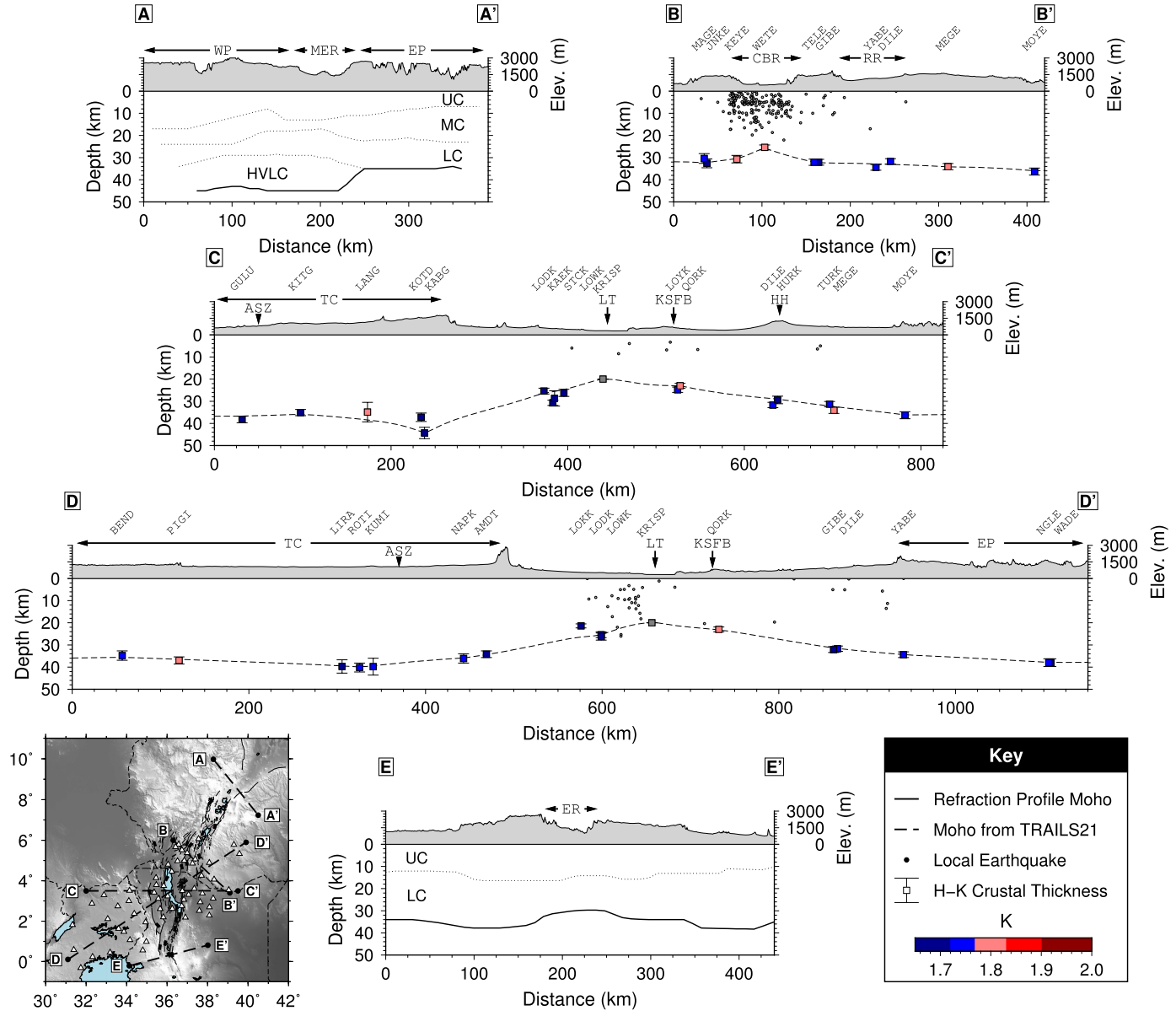

Fig. 4. Cross sections through various sectors of the East African rift crust. Profile orientations are shown on the bottom left map. **A-A'**: the wide-angle seismic line of Maguire et al. (2006) through the northern Main Ethiopian Rift. HVLC: High velocity lower crust. WP: Western plateau. MER: Main Ethiopian Rift. EP: Eastern Plateau. **B-B'**: Southernmost Ethiopia. Local earthquakes from Musila et al. (2022). CBR: Chew Bahir Rift. RR: Ririba Rift. **C-C' and D-D'**: from the Tanzania craton, through the Turkana Depression, and onto the Eastern Ethiopian Plateau. Grey squares: KRISP result from Mechie et al. (1997). LT: Lake Turkana. KSFB: Kino Sogo Fault Belt. HH: Huri Hills. **E-E'**: the KRISP wide-angle seismic line of Braile et al. (1994) through the Eastern Rift (ER). This profile is outside our array and hence microearthquake activity is unknown.

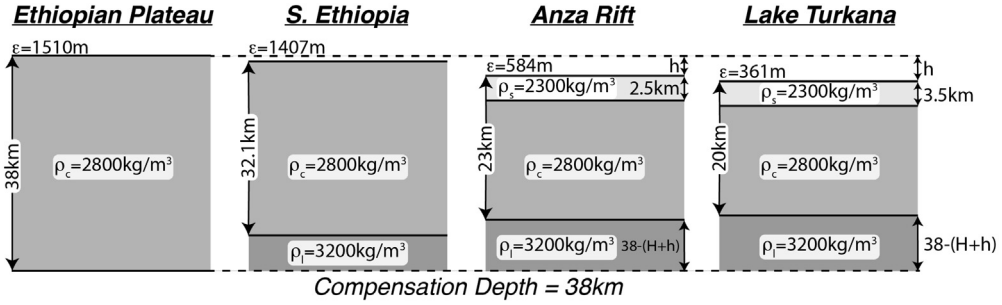

Fig. 5. Schematic 1D isostasy calculations with associated densities and layer thicknesses. Compensation depth of 38 km is the crustal thickness of the eastern Ethiopian plateau from station NGLE. ϵ is observed elevation, ρ_s, ρ_c and ρ_l are densities of sediments, crust and lithospheric mantle, respectively. H is calculated crustal thickness of each scenario and h is the expected elevation difference between an isostatic scenario and the Ethiopian plateau reference.

Table 3
Isostasy mass balance layer thickness and expected elevation differences. *Diff* is the difference between expected elevation difference and the observed elevation difference. ϵ is elevation, H_C is crustal thickness, H_S is sediment thickness. We assume sediment, crustal and lithospheric mantle densities of 2300 kg/m^3, 2800 kg/m^3 and 3200 kg/m^3, respectively.

Region	ϵ (m)	H_C (km)	H_S (km)	Exp. ϵ (m)	Obs. ϵ (m)	Diff. (m)
Ethiopian Plateau	1510	38	0	-	-	-
Southern Ethiopia	1407	32.1	0	738	103	635
Anza Rift	584	23	2.5	1484	926	558
Lake Turkana	361	20	3.5	1703	1149	554

like HURK are insensitive to potentially-localized magmatic plumbing systems, with or without present-day melt, directly below individual volcanoes. Our generally low V_P/V_S ratios, however, confirm that the Turkana Depression crust, at least in the areas where we have stations, is lacking in present-day melt and large volumes of mafic intrusions. Additionally, the independence of the phase conversions as a function of back-azimuth (an observation corroborated by the generally high CCC values across the network; Fig. S5c) at many of our stations (e.g., DILE; Fig. 2f and 2g) likely points towards an absence of highly anisotropic melt, for which there is significant evidence further north in the central and northern MER (e.g., Kendall et al., 2006).

Bulk crustal V_P/V_S ratios are not the only proxy for crustal modification via melt intrusion. Lower crustal intrusions blur the boundary between relatively fast wavespeed mantle and slow wavespeed crust, suppressing the amplitude of *Ps* Moho conversions in receiver functions, particularly at high frequencies (e.g., Ogden et al., 2019). Six good quality H-κ results (stations DILE, LODK, LOKK, TURE, TURK, QORK: Fig. 3a) in the Turkana Depression emerge using relatively high-frequency receiver functions ($\geq$1.3 Hz), and for which high ACE values are also associated (Fig. S5, Table S1) at all frequencies in the 0.4–2 Hz range (e.g., Fig. 2d). This means the thick (8–12 km) lower crustal intrusion layer observed in wide-angle data (Maguire et al., 2006) and coincident receiver function analysis (Ogden et al., 2019) below the Ethiopian plateau likely does not exist below the Turkana Depression. Corroborating this view, the KRISP wide-angle seismic profile (Mechie et al., 1997) only features a thin ($\leq$2 km), lower crustal intrusion layer below northernmost Lake Turkana, likely associated with the southernmost extent of Eocene flood basaltic magmatism in the region.

Stretching factors are another way to address questions concerning magma-assisted rifting. Wide-angle seismic profiles across the MER to the north (EAGLE, Fig. 4, profile A-A'; Maguire et al., 2006) and the Eastern Rift to the south of the Turkana Depression (KRISP: Fig. 4 profile, E-E'; Braile et al., 1994) show that crustal thinning is minimal (β = 1.1–1.3) below these narrow, magmatically-active rift zones in which significant extension is known to have been achieved via dyke intrusion. In contrast, $\beta \geq 1.9$ in both the Lokichar basin (where EAR extension began in the Turkana Depression in Oligo-Miocene times), and in the Lake Turkana basin. Our results indicate that extension-related magma intrusion has not altered the crust pervasively in either Mesozoic or Miocene-Recent rifting throughout large parts of the study area. Likewise, the area appears to have been relatively unaffected by initial flood magmatism ~45-35 Ma. The evolved nature of lavas from the Turkana and Suguta rift zones (e.g., Rooney et al., 2022), and the multiple dikes imaged in reflection profiles (e.g., Muirhead et al., 2022) indicate that these areas are experiencing strain localization by magma intrusion. This interpretation is consistent with large spatial gaps in $M > 5$ earthquakes in the Turkana Depression region.

In summary, with the caveat that we lack good quality H-κ results from stations immediately to the west of and beneath Lake Turkana, the lack of elevated V_P/V_S ratios associated with either present-day melt or large volumes of cooled gabbroic intrusions, coupled with the region's generally-high β factors, points strongly towards a scenario in which mechanical (faulting and ductile plate stretching), not magmatic, extension processes have been dominant in the Turkana Depression until recently. The magma-assisted rifting that is now underway below Lake Turkana and Suguta, is likely a very recent (<1 Ma) phenomenon, as has been suggested on the basis of petrological analysis of Quaternary lavas erupting along the lake (e.g., Muirhead et al., 2022; Rooney et al., 2022).

6.3. Strain localization in northern Uganda and southern Ethiopia

Within northern Uganda, a consistent ~3 km step in crustal thickness across the Precambrian Aswa shear zone (Fig. 3b), which was not noted in the earlier study of Wang et al. (2022), attests to the region being shielded from all Phanerozoic rifting phases affecting the Turkana Depression to the east. In southernmost Ethiopia, stations KEYE, JNKE, TELE, GIBE, YABE, and MEGE have Moho depths 30.4–34.4 km, some 4–7 km thinner than below station NGLE (38 km) on the eastern Ethiopian plateau. To first order, this corroborates the observation that south of ~7°N, Miocene-to-Recent extensional faulting has developed across a broad zone from the Omo Valley in the west to the Pliocene Ririba Rift in the east (Fig. 1; e.g., Ebinger et al., 2000). Moho depth at station DILE within the Ririba Rift is similar to nearby stations MEGE and GIBE that are outside of the rift ($\beta = 1.01$). This corroborates fault mapping and volcanic edifice studies (Corti et al., 2019; Franceschini et al., 2020) that consider the Ririba Rift a zone of negligible Pliocene-to-Pleistocene extension; seismicity is also notably lacking there (Fig. 4: B-B'; Musila et al., 2022).

Crustal thinning in southernmost Ethiopia is particularly pronounced below the Chew Bahir Rift, where $H_{WETE} = 25.4$ km and associated ~1.6 km of basin infill (Doherty et al., 2013) yields $\beta = 1.35$–1.60 (Table 2). With the caveat that the un-sampled, low-lying Omo Valley to the west may mark a similar zone of crustal thinning, seismicity and thus the present day locus of strain appears to be localized to the Chew Bahir Rift.

Intriguingly, broadly-rifted southernmost Ethiopia, which contrasts the narrow MER rift sectors to the north, has developed above a tomographically-imaged, narrow, high mantle wavespeed band, interpreted as refractory Proterozoic lithosphere (Kounoudis et al., 2021). Pre-rift lithospheric mantle heterogeneity, dating as far back as supercontinent assembly therefore appears to have exerted control on strain localization in southern Ethiopia. Below the Turkana Depression to the south, Cretaceous (130–80 Ma) and Paleogene (66–50 Ma) extension phases are also expected to have affected the crust (e.g., Morley et al., 1992; Ebinger et al., 2000), with important implications for subsequent Miocene-Recent EAR strain localization. We explore this issue in the next section.

6.4. Implications for Miocene-Recent strain development in the Turkana Depression

Moho depths are shallow below the Lokichar Basin (H_{LOKK} = 21.2 km: Fig. 3b), where EAR-related extension in the Turkana Depression initiated to the west of present-day Lake Turkana during

Oligocene-Miocene times (Morley et al., 1992). The Lokichar Basin is characterized by ≤2 km upper Miocene and Pliocene basin infill, deposited concomitant with the development of the Lokichar fault (Fig. 1b; Schofield et al., 2021). These overlie ∼780 m Mid-Miocene volcanics, and older Mid-Miocene-to-Paleogene strata that do not thicken towards the fault, implying deposition prior to the development of EAR extension. Basin analysis studies have, on the strength of such evidence, estimated ≥12 km of crustal thinning below the region (Morley et al., 1999). Assuming $H_{AMDT} = 34.2$ km for pre-Cenozoic crustal thickness, and correcting for 3.5 km basin infill (Schofield et al., 2021), this translates to $\beta \geq 1.9$ (Table 2).

The shortest connection between the narrower zones of active extension in the Chew Bahir Rift in Ethiopia and the Suguta Valley Rift in Kenya (Fig. 1), is through the ≤3 Ma KSFB (Vétel et al., 2005) to the east of Lake Turkana (Fig. 1), where we find evidence for thin crust ($H_{QORK} = 23$ km; Figs. 3 and 4). Seismicity and GPS data (Knappe et al., 2020) indicate present-day strain is localized to the west of the KSFB below Lake Turkana (Fig. 4: C-C', D-D'), consistent with structural geological observations that the small-offset (<100 m) faults of the ∼3 Ma-Recent KSFB have accommodated little EAR-related extension (Vétel et al., 2005). Strong gravity lows (Sippel et al., 2017) below the belt are interpreted as Anza Rift-related sedimentary basins, implying much of the observed crustal thinning developed during Mesozoic times. A clear picture thus emerges from our work: Oligocene-to-Recent rifting in the Turkana Depression has developed best in areas affected the least by earlier episodes of rifting.

The recent mantle tomographic inversion study of Kounoudis et al. (2021) revealed relatively fast wavespeeds at lithospheric depths below the northern KSFB. One hypothesis for the failure of present-day rifting to establish more successfully there is that post-Mesozoic plate cooling following crustal thinning during Anza rift development has left the KSFB lithosphere with a smaller crust:mantle ratio than its relatively un-stretched surroundings. Cenozoic strain has therefore localized to weaker zones of still-thick crust. Any magmatism during Anza rifting, or associated with subsequent Miocene-Recent volcanism, would also have rendered the underlying lithosphere stronger via dehydration of the mantle lithosphere. A strong lithospheric mantle below Anza rifted zones may therefore now be suppressing strain localization through the KSFB region. In a similar vein, strong lithosphere associated with the Anza rifting to the east of the KSFB may have contributed to the inability of Ririba rifting to develop south across the Turkana Depression.

The hypothesis that earlier, failed rift episodes can render the lithosphere more, not less, refractory with or without older heterogeneity (imparted, for example, during supercontinent assembly), has important implications for rifting models in any region like Turkana where multiple rifting episodes are superposed.

7. Conclusions

We present new receiver function constraints on Moho depth and bulk crustal V_P/V_S ratio below the Turkana Depression and neighboring northern Uganda using H and κ constraints from a combined network of 37 reliable seismograph stations. Moho depths reduce from ∼40 km on the Ethiopian Plateau and northern Uganda to ∼20 km below Lake Turkana, ∼21.4 km below the Lokichar Basin, and ∼23 km beneath the KSFB. Simple mass balance calculations that show the Turkana Depression is ∼550 m higher than expected compared to the eastern Ethiopian plateau. Crustal thinning, imparted during multiple, superposed rift phases therefore explains the low elevation of the Turkana Depression, with no requirement for a reduction in mantle dynamic support.

Bulk crustal V_P/V_S across the study area is generally much lower (∼1.74) than below the magma-rich central and northern sectors of the MER and flood basalt-affected Ethiopian plateau to the north (V_P/V_S >1.8). These observations, coupled with generally high stretching factors ($\beta \leq 2.11$), suggest that past-extension has been dominated by faulting and plate stretching, not magma intrusion. However, geochemical and seismicity studies confirm that magma-assisted rifting is presently ongoing below the Lake Turkana and Suguta basins, as marked by active volcanoes along the rift axis (e.g., Melnick et al., 2012; Rooney et al., 2022; Musila et al., 2022).

Although Cenozoic rifting in southern Ethiopia has developed over a broad region, EAR extension appears to have localized to the Chew Bahir Rift ($H_{WETE} = 25.4$ km). There is no evidence for pronounced crustal thinning below the Ririba Rift or Usno Basin. Thin crust ($H_{QORK} = 23$ km) in the Kino Sogo Fault Belt to the east of Lake Turkana is not easily explained by Cenozoic EAR rifting: faulting there is young (<3 Ma) and small-offset (<100 m), implying the observed thinning occurred in Mesozoic times during Anza rift development. Instead EAR rifting initially developed in basins with ≥2.5 km of Cenozoic basin fill to the west of Lake Turkana.

Despite the shortest connection between focused thinning in the Chew Bahir Rift in southern Ethiopia and the Suguta Valley to the south being through the KSFB, seismicity and GPS data show that extension is instead localized to the west below Lake Turkana. Fast wavespeeds, imaged by recent mantle tomographic studies of the Depression (Kounoudis et al., 2021) below the northern KSFB, attest to a strong present-day mantle lithosphere now playing an important role in governing the locus of strain: crustal thinning during failed Anza rifting is expected to have rendered the thermally re-equilibrated lithosphere stronger on account of its smaller crust-to-mantle ratio, and nominal mantle dehydration either during the earlier rifting phase or via subsequent Miocene-Recent volcanism.

CRediT authorship contribution statement

C.S. Ogden: Data curation, Formal analysis, Investigation, Methodology, Software, Visualization, Writing – original draft. **I.D. Bastow:** Conceptualization, Funding acquisition, Investigation, Methodology, Project administration, Resources, Software, Supervision, Visualization, Writing – original draft. **C. Ebinger:** Conceptualization, Funding acquisition, Investigation, Project administration, Writing – original draft. **A. Ayele:** Funding acquisition, Project administration, Writing – original draft. **R. Kounoudis:** Data curation, Investigation, Writing – original draft. **M. Musila:** Investigation, Visualization, Writing – original draft. **R. Bendick:** Conceptualization, Funding acquisition, Investigation, Project administration, Writing – original draft. **N. Mariita:** Funding acquisition, Project administration, Writing – original draft. **G. Kianji:** Funding acquisition, Investigation, Project administration, Writing – original draft. **T.O. Rooney:** Writing – original draft. **G. Sullivan:** Visualization, Writing – original draft. **B. Kibret:** Investigation, Writing – original draft.

Declaration of competing interest

The authors declare that they have no known competing financial interests or personal relationships that could have appeared to influence the work reported in this paper.

Data availability

The broadband seismograph data will be available in June 2023 for Kenyan TRAILS stations, June 2024 for Ethiopian TRAILS stations and all other data is already available via IRIS.

Acknowledgements

We thank editor J-P. Avouac and two anonymous reviewers for their insightful comments. The SEIS-UK data management facility (Brisbourne, 2012) provided instruments deployed in southern Ethiopia (Bastow, 2019) with V. Lane, D. Daly and L. Finch providing invaluable support. The seismic instruments deployed in Kenya (Ebinger, 2018) were provided by the Incorporated Research Institutions for Seismology (IRIS) through the PASSCAL Instrument Center at New Mexico Tech. Data collected will be available through the IRIS Data Management Center. The facilities of the IRIS Consortium are supported by the National Science Foundation's Seismological Facilities for the Advancement of Geoscience (SAGE) Award under Cooperative Support Agreement EAR-1851048. The facilities of IRIS Data Services, and specifically the IRIS Data Management Center, were used for access to waveforms, related metadata, and/or derived products used in this study for the ZP (Nyblade, 2007) and XW (Nyblade, 2017) networks. Seismic data for network GE (GEOFON, 1993) were obtained from the GEOFON data centre of the GFZ German Research Centre for Geosciences. M. Karanja, S. Mwangi, M. Wanyaga, B. Onguso, B., and S. Alemayehu assisted with fieldwork. J. Mechie and D. Cornwell kindly provided access to data from the KRISP and EAGLE projects, respectively. We acknowledge collaboration with the Universities of Nairobi and Addis Ababa, including their help establishing the TRAILS network. C. Ogden and I. Bastow acknowledge support from Natural Environment Research Council grant number NE/S014136/1. R. Kounoudis is funded by an Imperial College President's PhD Scholarship. C. Ebinger acknowledges NSFGEO-NERC award 1824417.

Appendix A. Supplementary material

Supplementary material related to this article can be found online at https://doi.org/10.1016/j.epsl.2023.118088.

References

Bastow, I., 2019. Turkana Rift Arrays to Investigate Lithospheric Strains (TRAILS) - UK component, International Federation of Digital Seismograph Networks. Other/Seismic Network. https://doi.org/10.7914/SN/9A_2019.

Bastow, I., Stuart, G., Kendall, J.-M., Ebinger, C., 2005. Upper-mantle seismic structure in a region of incipient continental breakup: northern Ethiopian rift. Geophys. J. Int. 162, 479–493. https://doi.org/10.1111/j.1365-246X.2005.02666.x.

Benoit, M., Nyblade, A., Pasyanos, M., 2006. Crustal thinning between the Ethiopian and East African Plateaus from modeling Rayleigh wave dispersion. Geophys. Res. Lett. 33 (13), L13301. https://doi.org/10.1029/2006GL025687.

Boyce, A., Bastow, I.D., Cottar, S., Kounoudis, R., Guilloud De Courbeville, J., Caunt, E., Desai, S., 2021. AFRP20: new P-wavespeed model for the African mantle reveals two whole-mantle plumes below East Africa and neoproterozoic modification of the Tanzania craton. Geochem. Geophys. Geosyst. 22 (3), e2020GC009302. https://doi.org/10.1029/2020GC009302.

Braile, L., Wang, B., Daudt, C., Keller, G., Patel, J., 1994. Modeling the 2-D seismic velocity structure across the Kenya rift. Tectonophysics 236 (1–4), 251–269. https://doi.org/10.1016/0040-1951(94)90179-1.

Brisbourne, A., 2012. How to store and share geophysical data. Astron. Geophys. 53 (4), 19–20.

Brune, S., Corti, G., Ranalli, G., 2017. Controls of inherited lithospheric heterogeneity on rift linkage: numerical and analog models of interaction between the Kenyan and Ethiopian rifts across the Turkana Depression. Tectonics 36 (9), 1767–1786. https://doi.org/10.1002/2017TC004739.

Cornwell, D., Mackenzie, G., England, R., Maguire, P., Asfaw, L., Oluma, B., 2006. Northern main Ethiopian rift crustal structure from new high-precision gravity data. In: Yirgu, G., Ebinger, C.J., Maguire, P.K.H. (Eds.), The Afar Volcanic Province Within the East African Rift System. In: Geol. Soc. Lond. Spec. Pub., vol. 256, pp. 307–321.

Corti, G., Cioni, R., Franceschini, Z., Sani, F., Scaillet, S., Molin, P., Isola, I., Mazzarini, F., Brune, S., Keir, D., Erbello, A., Muluneh, A., Illsley-Kemp, F., Glerum, A., 2019. Aborted propagation of the Ethiopian rift caused by linkage with the Kenyan rift. Nat. Commun. 10 (1), 1–11. https://doi.org/10.1038/s41467-019-09335-2.

Cunningham, E., Lekic, V., 2019. Constraining crustal structure in the presence of sediment: a multiple converted wave approach. Geophys. J. Int. 219 (1), 313–327.

Davidson, A., Rex, D., 1980. Age of volcanism and rifting in southwestern Ethiopia. Nature 283, 657–658. https://doi.org/10.1038/283657a0.

Doherty, J., Bennett, S., Martini, F., Melady, G., Simpson, K., Rogers, E., 2013. Integrated geophysical exploration in a frontier Basin-South Omo, Ethiopia. In: 75th EAGE Conference & Exhibition Incorporating SPE EUROPEC 2013. European Association of Geoscientists & Engineers, cp-348.

Ebinger, C., 2018. Turkana Rift Arrays to Investigate Lithospheric Strains (TRAILS) - USA component, International Federation of Digital Seismograph Networks. Other/Seismic Network. https://doi.org/10.7914/SN/Y1_2018.

Ebinger, C., Casey, M., 2001. Continental breakup in magmatic provinces: an Ethiopian example. Geology 29, 527–530. https://doi.org/10.1130/0091-7613(2001)029<0527:CBIMPA>2.0.CO;2.

Ebinger, C., Sleep, N., 1998. Cenozoic magmatism throughout East Africa resulting from impact of a single plume. Nature 395, 788–791. https://doi.org/10.1038/27417.

Ebinger, C., Yemane, T., Harding, D., Tesfaye, S., Kelley, S., Rex, D., 2000. Rift deflection, migration, and propagation: linkage of the Ethiopian and Eastern rifts, Africa. Bull. Seismol. Soc. Am. 112 (2), 163–176. https://doi.org/10.1130/0016-7606(2000)112<163:RDMAPL>2.0.CO;2.

Emishaw, L., Abdelsalam, M.G., 2019. Development of late Jurassic-early Paleogene and Neogene-Quaternary rifts within the Turkana Depression, East Africa from satellite gravity data. Tectonics 38 (7), 2358–2377. https://doi.org/10.1029/2018TC005389.

Franceschini, Z., Cioni, R., Scaillet, S., Corti, G., Sani, F., Isola, I., Mazzarini, F., Duval, F., Erbello, A., Muluneh, A., et al., 2020. Recent volcano-tectonic activity of the Ririba rift and the evolution of rifting in South Ethiopia. J. Volcanol. Geotherm. Res. 403, 106,989. https://doi.org/10.1016/j.jvolgeores.2020.106989.

Fritz, H., Abdelsalam, M., Ali, K., Bingen, B., Collins, A., Fowler, A., Ghebreab, W., Hauzenberger, C., Johnson, P., Kusky, T., Macey, P., Muhongo, S., Stern, R.J., Viola, G., 2013. Orogen styles in the East African Orogen: a review of the Neoproterozoic to Cambrian tectonic evolution. J. Afr. Earth Sci. 86, 65–106. https://doi.org/10.1016/j.jafrearsci.2013.06.004.

Furman, T., Kaleta, K., Bryce, J., Hanan, B., 2006. Tertiary mafic lavas of Turkana, Kenya: constraints on East African plume structure and the occurrence of high-μ volcanism in Africa. J. Petrol. 47 (6), 1221–1244. https://doi.org/10.1093/petrology/egl009.

GEOFON, 1993. GEOFON seismic network, GFZ data services. Other/Seismic Network. https://doi.org/10.14470/TR560404.

Haileab, B., Brown, F.H., McDougall, I., Gathogo, P.N., 2004. Gombe group basalts and initiation of Pliocene deposition in the Turkana Depression, northern Kenya and southern Ethiopia. Geol. Mag. 141 (1), 41–53. https://doi.org/10.1017/S001675680300815X.

Halldórsson, S., Hilton, D., Scarsi, P., Abebe, T., Hopp, J., 2014. A common mantle plume source beneath the entire East African Rift System revealed by coupled helium-neon systematics. Geophys. Res. Lett. 41 (7), 2304–2311. https://doi.org/10.1002/2014GL059424.

Hendrie, D., Kusznir, N., Morley, C., Ebinger, C., 1994. Cenozoic extension in northern Kenya: a quantitative model of rift basin development in the Turkana region. Tectonophysics 236 (1–4), 409–438. https://doi.org/10.1016/0040-1951(94)90187-2.

Hilton, D., Halldórsson, S., Barry, P., Fischer, T., de Moor, J., Ramirez, C., Mangasini, F., Scarsi, P., 2011. Helium isotopes at Rungwe Volcanic Province, Tanzania, and the origin of East African plateaux. Geophys. Res. Lett. 38 (21). https://doi.org/10.1029/2011GL049589.

Kendall, J.-M., Pilidou, S., Keir, D., Bastow, I., Stuart, G., Ayele, A., 2006. Mantle upwellings, melt migration and the rifting of Africa: insights from seismic anisotropy, in the Afar Volcanic Province within the East African Rift System. In: Yirgu, G., Ebinger, C.J., Maguire, P.K.H. (Eds.), Geol. Soc. (Lond.) Spec. Publ. 259, 271–293.

Keranen, K., Klemperer, S., Gloaguen, R., EAGLE Working Group, 2004. Three-dimensional seismic imaging of a protoridge axis in the main Ethiopian rift. Geology 32, 949–952. https://doi.org/10.1130/G20737.1.

Key, R., Rop, B., Rundle, C., 1987. The development of the late Cenozoic alkali basaltic Marsabit shield volcano, northern Kenya. J. Afr. Earth Sci. 6 (4), 475–491. https://doi.org/10.1016/0899-5362(87)90089-3.

Knappe, E., Bendick, R., Ebinger, C.J., Birhanu, Y., Lewi, E., Floyd, M., King, R., Kianji, G., Mariita, N., Temtime, T., Waktola, B., Deresse, B., Musila, M., Kanoti, J., Perry, M., 2020. Accommodation of East African Rifting across the Turkana Depression. J. Geophys. Res. e2019JB018469. https://doi.org/10.1029/2019JB018469.

Kogan, L., Fisseha, S., Bendick, R., Reilinger, R., McClusky, S., King, R., Solomon, T., 2012. Lithospheric strength and strain localization in continental extension from observations of the East African Rift. J. Geophys. Res. 117 (B3). https://doi.org/10.1029/2011JB008516.

Kounoudis, R., Bastow, I., Ebinger, C., Ogden, C., Ayele, A., Bendick, R., Mariita, N., Kianji, G., Wigham, M., Musila, G., Abera, B., 2021. Body-wave tomographic imaging of the Turkana Depression: implications for rift development and plume-lithosphere interactions. Geochem. Geophys. Geosyst. 22, e2021GC009782. https://doi.org/10.1029/2021GC009782.

Ligorrìa, J., Ammon, C., 1999. Iterative deconvolution and receiver-function estimation. Bull. Seismol. Soc. Am. 89 (5), 1395–1400. https://doi.org/10.1785/BSSA0890051395.

Mackenzie, G., Thybo, H., Maguire, P., 2005. Crustal velocity structure across the Main Ethiopian Rift: results from 2-dimensional wide-angle seismic modelling. Geophys. J. Int. 162, 994–1006. https://doi.org/10.1111/j.1365-246X.2005.02710.x.

Maguire, P., Keller, G., Klemperer, S., Mackenzie, G., Harder, S., OReilly, B., Thybo, H., Asfaw, L., Khan, M., Amha, M., 2006. Crustal structure of the northern Main Ethiopian Rift from the EAGLE controlled-source survey; a snapshot of incipient lithospheric break-up, in the Afar Volcanic Province within the East African Rift System. In: Yirgu, G., Ebinger, C.J., Maguire, P.K.H. (Eds.), Geol. Soc. (Lond.) Spec. Publ. 259, 271–293. https://doi.org/10.1144/GSL.SP.2006.259.01.21.

Marty, B., Pik, R., Yirgu, G., 1996. Helium isotopic variations in Ethiopian plume lavas: nature of magmatic sources and limit on lower mantle contribution. Earth Planet. Sci. Lett. 144 (1), 223–237. https://doi.org/10.1016/0012-821X(96)00158-6.

Mechie, J., Keller, G., Prodehl, C., Khan, M., Gaciri, S., 1997. A model for the structure, composition and evolution of the Kenya rift. Tectonophysics 278, 95–119. https://doi.org/10.1016/S0040-1951(97)00097-8.

Melnick, D., Garcin, Y., Quinteros, J., Strecker, M.R., Olago, D., Tiercelin, J.-J., 2012. Steady rifting in northern Kenya inferred from deformed Holocene lake shorelines of the Suguta and Turkana basins. Earth Planet. Sci. Lett. 331, 335–346. https://doi.org/10.1016/j.epsl.2012.03.007.

Moore, H., Davidson, A., 1978. Rift structure in southern Ethiopia. Tectonophysics 46, 159–173. https://doi.org/10.1016/0040-1951(78)90111-7.

Morley, C., Wescott, W., Stone, D., Harper, R., Wigger, S., Karanja, F., 1992. Tectonic evolution of the northern Kenyan Rift. J. Geol. Soc. 149 (3), 333. https://doi.org/10.1144/gsjgs.149.3.033.

Morley, C., Karanja, F., Wescott, W., Stone, D., Harper, R., Wigger, S., Day, R., 1999. AAPG studies in geology# 44, Chapter 2: geology and geophysics of the Western Turkana Basins, Kenya. In: AAPG Special Volume.

Muirhead, J.D., Fischer, T.P., Oliva, S.J., Laizer, A., van Wijk, J., Currie, C.A., Lee, H., Judd, E.J., Kazimoto, E., Sano, Y., Takahata, N., Tiberi, C., Foley, S.F., Dufek, J., Reiss, M.C., Ebinger, C.J., 2020. Displaced cratonic mantle concentrates deep carbon during continental rifting. Nature 582 (7810), 67–72. https://doi.org/10.1038/s41586-020-2328-3.

Muirhead, J.D., Scholz, C.A., Rooney, T., 2022. Transition to magma-driven rifting in the South Turkana basin: part I. J. Geol. Soc. 179, jgs2021–159. https://doi.org/10.1144/jgs2021-159.

Musila, M., Ebinger, C., Sullivan, G., Bastow, I., Bendick, R., Ogden, C., Kounoudis, R., 2022. Strain accommodation during continental rifting: mantle lithosphere matters. In: AGU Fall Meeting Abstracts.

Nyblade, A., 2007. Africa array - Uganda/Tanzania, international federation of digital seismograph networks. Other/Seismic Network. https://doi.org/10.7914/SN/ZP_2007.

Nyblade, A., 2017. Broadband seismic experiment in NE Uganda to investigate plume-lithosphere interactions, international federation of digital seismograph networks. Other/Seismic Network. https://doi.org/10.7914/SN/XW_2017.

Ogden, C., Bastow, I., 2022. The crustal structure of the Anatolian Plate from receiver functions and implications for the uplift of the central and eastern Anatolian plateaus. Geophys. J. Int. 229 (2), 1041–1062. https://doi.org/10.1093/gji/ggab513.

Ogden, C., Bastow, I., Gilligan, A., Rondenay, S., 2019. A reappraisal of the H-κ stacking technique: implications for global crustal structure. Geophys. J. Int. 219 (3), 1491–1513. https://doi.org/10.1093/gji/ggz364.

Ogden, C., Keir, D., Bastow, I., Ayele, A., Marcou, S., Woodward, A., Abera, B., Gudbrandsson, S., 2021. Seismicity and crustal structure of the Southern Main Ethiopian Rift: new evidence from Lake Abaya. Geochem. Geophys. Geosyst. 22, e2021GC009831. https://doi.org/10.1029/2021GC009831.

Park, Y., Nyblade, A., 2006. P-wave tomography reveals a westward dipping low velocity zone beneath the Kenya Rift. Geophys. Res. Lett. 33 (7). https://doi.org/10.1029/2005GL025605.

Ritsema, J., Deuss, A., van Heijst, H., Woodhouse, J., 2011. S40RTS: a degree-40 shear-velocity model for the mantle from new Rayleigh wave dispersion, teleseismic traveltime and normal-mode splitting function measurements. Geophys. J. Int. 184 (3), 1223–1236. https://doi.org/10.1111/j.1365-246X.2010.04884.x.

Rogers, N., Macdonald, R., Fitton, J., George, R., Smith, R., Barreiro, B., 2000. Two mantle plumes beneath the East African rift system: Sr, Nd and Pb isotope evidence from Kenya Rift basalts. Earth Planet. Sci. Lett. 176, 387–400. https://doi.org/10.1016/S0012-821X(00)00012-1.

Rooney, T., Herzberg, C., Bastow, I., 2012. Elevated mantle temperature beneath East Africa. Geology 40 (G32382R1), 27–40. https://doi.org/10.1130/G32382.1.

Rooney, T., Lavigne, A., Svoboda, C., Girard, G., Yirgu, G., Ayalew, D., Kappelman, J., 2017. The making of an underplate: pyroxenites from the Ethiopian lithosphere. Chem. Geol. 455, 264–281. https://doi.org/10.1016/j.chemgeo.2016.09.011.

Rooney, T.O., 2020a. The Cenozoic magmatism of East Africa: part II–Rifting of the mobile belt. Lithos 360, 105,291. https://doi.org/10.1016/j.lithos.2019.105291.

Rooney, T.O., 2020b. The Cenozoic magmatism of East Africa: part III–rifting of the craton. Lithos 360, 105,390. https://doi.org/10.1016/j.lithos.2020.105390.

Rooney, T.O., 2020c. The Cenozoic magmatism of East Africa: part V–magma sources and processes in the East African Rift. Lithos 360, 105,296. https://doi.org/10.1016/j.lithos.2019.105296.

Rooney, T.O., Wallace, P.J., Muirhead, J.D., Chiasera, B., Steiner, R.A., Girard, G., Karson, J.A., 2022. Transition to magma-driven rifting in the South Turkana basin: part 2. J. Geol. Soc., 2021-160. https://doi.org/10.1144/jgs2021-160.

Saalmann, K., Mänttäri, I., Nyakecho, C., Isabirye, E., 2016. Age, tectonic evolution and origin of the Aswa Shear Zone in Uganda: activation of an oblique ramp during convergence in the East African Orogen. J. Afr. Earth Sci. 117, 303–330. https://doi.org/10.1016/j.jafrearsci.2016.02.002.

Schimmel, M., Paulssen, H., 1997. Noise reduction and detection of weak, coherent signal through phase-weighted stacks. Geophys. J. Int. 130, 497–505. https://doi.org/10.1111/j.1365-246X.1997.tb05664.x.

Schofield, N., Newton, R., Thackrey, S., Watson, D., Jolley, D., Morley, C., 2021. Linking surface and subsurface volcanic stratigraphy in the Turkana Depressionc of the East African Rift system. J. Geol. Soc. 178 (1). https://doi.org/10.1144/jgs2020-1.

Sippel, J., Meeßen, C., Cacace, M., Mechie, J., Fishwick, S., Heine, C., Scheck-Wenderoth, M., Strecker, M., 2017. The Kenya rift revisited: insights into lithospheric strength through data-driven 3-d gravity and thermal modelling. Solid Earth 8 (1), 45–81. https://doi.org/10.5194/se-8-45-2017.

Steiner, R.A., Rooney, T.O., Girard, G., Rogers, N., Ebinger, C.J., Peterson, L., Phillips, R.K., 2021. Initial Cenozoic magmatic activity in East Africa: new geochemical constraints on magma distribution within the Eocene continental flood basalt province. Geol. Soc. (Lond.) Spec. Publ. 518. https://doi.org/10.1144/SP518-2020-262.

Stuart, G., Bastow, I., Ebinger, C., 2006. Crustal structure of the northern Main Ethiopian rift from receiver function studies. In: Yirgu, G., Ebinger, C.J., Maguire, P.K.H. (Eds.), The Afar Volcanic Province Within the East African Rift System. In: Geol. Soc. Lond. Spec. Pub., vol. 259, pp. 271–293.

Tugume, F., Nyblade, A., Julia, J., van der Meijde, M., 2013. Precambrian crustal structure in Africa and Arabia: evidence lacking for secular variation. Earth Planet. Sci. Lett. 609, 250–266. https://doi.org/10.1016/j.tecto.2013.04.027.

Vétel, W., Le Gall, B., Walsh, J.J., 2005. Geometry and growth of an inner rift fault pattern: the Kino Sogo Fault Belt, Turkana Rift (North Kenya). J. Struct. Geol. 27 (12), 2204–2222. https://doi.org/10.1016/j.jsg.2005.07.003.

Wang, T., Gao, S.S., Yang, Q., Chen, L., Liu, K.H., 2022. Lithospheric structure underneath the Archean Tanzania Craton and adjacent regions from a joint inversion of receiver functions and Rayleigh-wave phase velocity dispersion. Seismol. Res. Lett. 93 (3), 1753–1767. https://doi.org/10.1785/0220210296.

Whaler, K., Hautot, S., 2006. The electrical resistivity structure of the crust beneath the northern Ethiopian rift. In: Yirgu, G., Ebinger, C.J., Maguire, P.K.H. (Eds.), The Afar Volcanic Province Within the East African Rift System. In: Geol. Soc. Lond. Spec. Pub., vol. 256, pp. 293–305.

Wilson, M., Guiraud, R., 1992. Magmatism and rifting in Western and Central Africa, from Late Jurassic to recent times. Tectonophysics 213 (1–2), 203–225. https://doi.org/10.1016/0040-1951(92)90259-9.

Zhu, L., Kanamori, H., 2000. Moho depth variation in southern California from teleseismic receiver functions. J. Geophys. Res. 105 (B2), 2969–2980. https://doi.org/10.1016/S0012-821X(00)00101-1.